Generalized Rayleigh-Sommerfeld Diffraction Theory for Metasurface-Modulating Paraxial and Non-Paraxial Near-Field Pattern Estimation

HONGJUN CHU[1], **JIARAN QI**[1], **RUI WANG**[1,2], **AND JINGHUI QIU**[1]

[1]Department of Microwave Engineering, School of Electronics and Information Engineering, Harbin Institute of Technology, Harbin 150001, China
[2]China Research Institute of Radiowave Propagation, Xinxiang, China

Corresponding author: Jiaran Qi (qi.jiaran@hit.edu.cn)

ABSTRACT In this paper, different diffraction theories for estimating the diffraction field patterns modulated by metasurfaces are firstly revisited. Further reformulation of these theories is performed to better reveal their inherent mechanisms and differences. To compute the metasurface-modulating paraxial and/or non-paraxial diffraction field patterns within the near-field region, including the evanescent area, a universal pattern-propagation Eigenfactor is introduced to generalize Rayleigh-Sommerfeld diffraction theory. To investigate its applicability and accuracy, a representative monofocal metasurface with an ultrahigh numerical aperture of 0.96, together with two coplanar and non-coplanar multifocal holographic metasurfaces, are constructed as illustrative examples. Their near-field patterns are calculated by the generalized Rayleigh-Sommerfeld (GRS) diffraction integral and compared with those extracted by the finite-different time-domain full wave analysis, generalized Huygens-Fresnel principle, and Huygens's Principle. It is demonstrated that within the near-field region including the non-paraxial and evanescent area, the GRS diffraction integral provides the best and satisfactory agreement with the full wave simulation, and thus offers a more accurate and efficient tool for quantitative analysis and iterative optimization.

INDEX TERMS Metasurface, paraxial and non-paraxial near-field patterns, evanescent area, pattern-propagation Eigenfactor, focusing metasurface, passive millimeter-wave imaging.

I. INTRODUCTION

In recent years, versatile metasurfaces consisting of elaborately arranged subwavelength unit cells have sprung up as thin two-dimensional (2D) diffractive optical elements (DOE) or their electromagnetic (EM) analogs for flexibly shaping the EM fields by manipulating their phase, amplitude, and polarization [1]–[5]. Typical metasurface-based devices include flat lenses [6], [7], polarimeters [8], waveplates [9]–[11], absorbers [12], [13], and holograms [14], [15], where different methods have been applied to facilitate their synthetization, such as generalized sheet transition conditions [16]–[18], impedance surface theory [19], [20], and generalized laws of reflection and refraction [21]–[25]. As for the spatial field distribution within vicinity and far from the metasurface, the time-consuming full wave numerical simulation tends to be the most reliable choice, which requires heavy computational resources, greatly in turn affecting the design efficiency and making impossible the iterative optimization in e.g., holographic metasurface inversion. Therefore, how to accurately yet efficiently calculate the field distribution modulated by a given metasurface becomes an issue of practical significance.

To tackle this issue, diffraction theory and its variants are often adopted, which interpret the interference fields arising from fictitious sufficiently small secondary wave sources located within the diffraction aperture. Their applicability and accuracy of estimating the diffracted far-field by metasurface-based devices have been extensively studied and verified both theoretically and experimentally. The Huygens-Fresnel principle has been demonstrated as a design methodology to define the ideal surface impedance profile of a visible-band, wide-angle gradient metasurface for highly efficient back reflection [26]. Rayleigh-Sommerfeld diffraction integrals for the far-field region beyond the near zone behind metalens is adopted to calculate an abruptly

on-axis autofocusing cylindrically polarized laser beam [27]. In acoustics within far-field region (more than 10λ) the on-axis focusing field patterns of two metasurfaces are estimated by the acoustic Rayleigh-Sommerfeld diffraction integral [28]. The field distributions of two Fresnel reflective acoustic metasurfaces with numerical apertures (NA) of 0.71 and 0.45, and focal distances (*fd*) of 2λ and 4λ are numerically predicted by Huygens' Principle [29]. Modified Huygens-Fresnel principle is presented to rapidly compute the far-field transformations operated by a dielectric metasurface at the Q-band with fairly high accuracy compared to the full wave simulation [30]. The simplified Huygens-Fresnel principle is used to numerically compute the on-axis field profiles and evaluate the focal spot qualities within the paraxial area more than 20 mm away from the zoned fishnet metamaterial lens at 55 GHz [31].

Unfortunately, in these available reports only the paraxial far-field distributions are analyzed by the diffraction theory. As for the non-paraxial patterned fields especially within the subwavelength evanescent region, where many important metasurface-based applications are established, e.g., subwavelength near-field imaging [32], planar and stereo holography [33], [34], single-photon detection [35], immersion interference photolithography [36], [37], and near-field ptychography [38], it is not well studied yet whether the abovementioned diffraction theory can compute the near-field patterns with acceptable accuracy. If otherwise, it becomes thus an open question how to improve the degree of accuracy of the abovementioned methodologies when dealing with the metasurface-modulating non-paraxial near-field patterns. In this paper, we first revisit various forms of diffraction theories for estimating the field patterns emanating from the metasurfaces. We then provide a generalized version of Rayleigh-Sommerfeld diffraction theory (GRS) by introducing a universal pattern-propagation Eigenfactor, and meanwhile analyze the defects of available diffraction theories when dealing with the metasurface-modulating non-paraxial near-field patterns. To demonstrate its superiority, the near-field patterns of several monofocal and multifocal holographic metasurfaces as illustrative examples are computed, and compared with those extracted by the full wave analysis, Huygens-Fresnel principle without any approximations (referred to as generalized Huygens-Fresnel principle (GHF)), and Huygens's principle (HP).

It is noted that in practical implementations the metasurface-modulating non-paraxial near-fields are more likely of interest at low frequencies. Take near-field passive millimeter-wave focal plane array (PMMW-FPA) imaging as an example. PMMW-FPA imaging usually requires a focusing lens of high spatial resolution and wide field of view (FOV). To guarantee the resolution, the metasurface-lens with large NA are often required since the relatively large wavelength hinders the physical implementation of a sufficiently large aperture. Large NA and FOV thus indicates that an accurate yet efficient method to compute the non-paraxial near-fields of the metasurface-lens is of great

interest in this case. Therefore, in this paper, we set up the specific numerical experiments at millimeter-wave (MMW) band.

The following text of the paper is arranged as follows. Firstly, the GRS, together with the GHF and HP are formulated, whose physical interpretations are also given. Then, as illustrative examples, a typical focusing metasurface with ultrahigh $NA = 0.96$ and $fd = 0.58\lambda_0$ for the near-field PMMW-FPA imaging at 35 GHz is assembled. Its corresponding field patterns under normal and oblique illumination of a linearly polarized Gaussian plane-wave is investigated by the GRS, and compared with that extracted by the FDTD solver, the GHF, and the HP. Furthermore, another two multifocal holographic metasurfaces whose patterned fields are made up of four coplanar focal spots and three non-coplanar ones, respectively, are generated. Similar computation and comparison are conducted as well. Finally, discussion and concluding remarks are given.

II. FORMULATION OF THE GENERALIZED DIFFRACTION THEORY

The integral theorem of Helmholtz and Kirchhoff derived from Helmholtz equation and Green's theorem plays a significant role in the development of the scalar diffraction theory and its vector variants [39]–[42], since it allows $E(\boldsymbol{r})$, the field at observation point (x, y, z) is expressed in terms of $E(\boldsymbol{r}\prime)$ and its derivative $\nabla\prime E(\boldsymbol{r}\prime)$, the boundary values of the wave on any closed surface surrounding that point, which reads,

$$E(\boldsymbol{r}) = \frac{1}{4\pi} \oint_{S} [G(\boldsymbol{r}, \boldsymbol{r}\prime)\boldsymbol{n} \cdot \nabla\prime E(\boldsymbol{r}\prime) - E(\boldsymbol{r}\prime)\boldsymbol{n} \cdot \nabla\prime G(\boldsymbol{r}, \boldsymbol{r}\prime)]ds \tag{1}$$

where $E(\boldsymbol{r}\prime)$ represents the field at source point $(x\prime, y\prime, z\prime)$, $G(\boldsymbol{r}, \boldsymbol{r}\prime)$ is the Green's function which may be regarded as an auxiliary function chosen to solve the aforementioned problem, $\boldsymbol{n}$ denotes the inner normal vector on the closed surface S surrounding the observation point, and $\boldsymbol{r}$ and $\boldsymbol{r}\prime$ are the distance vectors from the origin point to the observation point (x, y, z) and the source point $(x\prime, y\prime, z\prime)$, respectively, as shown in Fig. 1.

To distinguish different forms of diffraction theory and meanwhile reveal their respective inherent mechanisms, we define the rest terms excluding the disturbance source $E(\boldsymbol{r}\prime)$ in the integral of (1) as the pattern-propagation Eigenfactor. It can be physically understood as an anisotropic "directivity pattern" associated with each disturbance source $E(\boldsymbol{r}\prime)$ on the diffraction aperture, implying their spatial complex field distribution characteristics. The difference among the aforementioned diffraction integrals just lies in this Eigenfactor.

A. GRS AND ITS PATTERN-PROPAGATION EIGENFACTOR
According to the Sommerfeld radiation condition and potential theory [39]–[42], the adopted Green's function $G(\boldsymbol{r}, \boldsymbol{r}\prime) = e^{jkR}/R - e^{jkR\prime}/R\prime$, is composed of two identical point sources
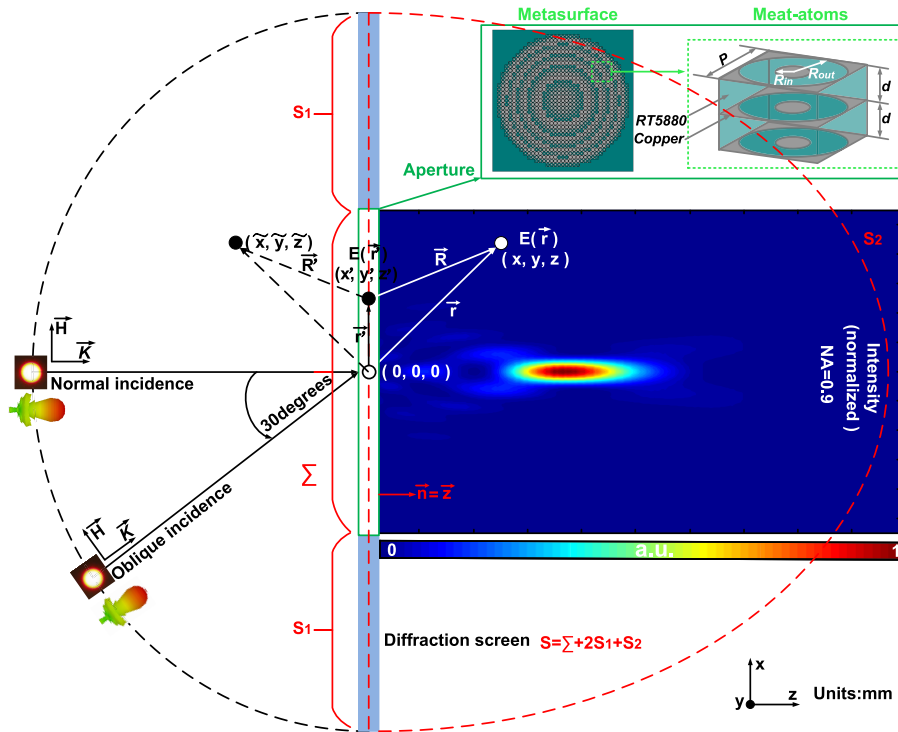
FIGURE 1. The 2D diffraction screen schematic diagram for the GRS and GHF in the Cartesian coordinate system. An illustrative focusing metasurface of NA = 0.9 and fd = 25 mm under normal illumination of a linearly polarized Gaussian plane-wave at 35 GHz and its electric-field-intensity pattern on the y = 0 plane estimated by the GRS. The unit cell (coaxial annular apertures (CAAs)) in the green dashed box is also inserted in the figure.

with the reversal phase as mirror image of each other at two sides of the metasurface, as shown in Fig. 1. According to (1), under the assumption of $kR \gg 1$, the conventional Rayleigh-Sommerfeld diffraction integral (CRS), which is often adopted to describe the diffracted fields after an obstacle or aperture, reads,

$$E(\boldsymbol{r}) = \iint_{\Sigma} E(\boldsymbol{r}')[\frac{1}{j\lambda}\cos(\boldsymbol{n},\boldsymbol{R})\frac{e^{jkR}}{R}]ds \quad (2)$$

where k is the wave number corresponding to the wavelength λ, $\boldsymbol{r} = \boldsymbol{r} - \boldsymbol{r'}$ with its module value of $R = |\boldsymbol{r} - \boldsymbol{r'}|$ is the distance vector from the source point $\boldsymbol{r'}$ to the observation point $\boldsymbol{r}$, $\boldsymbol{r'}$ and $R\prime$ are the mirror distance vector of $\boldsymbol{r}$ and its corresponding modulus, respectively, and the boundary surface $\sum$ is the aperture or obstacle, i.e., the zero-thickness metasurface here.

From (2), the pattern-propagation Eigenfactor of the CRS, i.e., the complex polynomial in square brackets, is formally identical to the far-field radiation expression of an oscillating dipole, so that this Eigenfactor can be regarded as its far-field radiation pattern. Obviously, the CRS inherently ignores the near-field effect of dipole, implying that it cannot capture the near-field information emerging from the metasurfaces. Based on this point, in this contribution we introduce an expanding pattern-propagation Eigenfactor covering not just far-field but the near-field of oscillating dipole to constructing a generalized diffraction integral, i.e., GRS, whose specific form reads as follows,

$$E(\boldsymbol{r}) = \iint_{\Sigma} E(\boldsymbol{r}')[\frac{1}{2\pi}(-jk + \frac{1}{R})\cos(\boldsymbol{n},\boldsymbol{R})\frac{e^{jkR}}{R}]ds \quad (3)$$

Obviously, the complex pattern-propagation Eigenfactor is perfectly consistent with the magnetic/electric field forms of the electric/magnetic dipole with only lagging or leading phase by $\pi/2$. This generalized Eigenfactor inherently accounts for the near-field effect of dipole, potentially showing that it remains valid in the computation of short-distance diffraction pattern from the metasurface. Thus, $E(\boldsymbol{r})$ may be described as the interference field at (x, y, z) arising from an infinity of fictitious dipole sources $E(\boldsymbol{r'})$ within the diffraction aperture, as denoted by (3). Here, it is noted that $E(\boldsymbol{r'})$ may be regarded as the complex amplitude of the modulated wavefront on the metasurface, containing the reference wavefront information from the field source and the disturbed complex amplitude information caused by itself.

B. GHF, HP AND THEIR PATTERN-PROPAGATION EIGENFACTOR

Similarly, the GHF (also known as modified Huygens-Fresnel principle) is derived from (1), and reads,

$$E(\boldsymbol{r}) = \iint_{\Sigma} E(\boldsymbol{r}')\{\frac{1}{4\pi}[(-jk + \frac{1}{R})\cos(\boldsymbol{n},\boldsymbol{R}) - jk]\frac{e^{jkR}}{R}\}ds$$

$$(4)$$

Here, the auxiliary Green's function $G(r, r') = e^{jkR}/R$ is selected to derive the GHF. Compared to the GRS, the pattern-propagation Eigenfactor in (4) contains an additive term $-jke^{jkR}/(2\pi R)$, inherently implying that the GHF takes into account the point source oscillation effect. Therefore, the computational field $E(r)$ may be construed as the result of oscillating dipoles together with point sources mutual interference under the field source $E(r')$ excitation.

In addition, according to Huygens' Principle, if the field source, $E(r')$ is incident on the aperture or obstacle, the field produced by this aperture or obstacle can be given by the surface integral reading as follows,

$$E(r) = \iint_{\Sigma} E(r') \frac{-j}{\lambda} \frac{e^{jkR}}{R} ds \qquad (5)$$

The pattern-propagation Eigenfactor in (5) is just point source irradiating the uniform spherical waves. Compared to the GRS and the GHF, it is obvious that the HP can be viewed as their simplified versions under the paraxial (it means $\cos(n, r) = 1$)) and far-field (it assumes $1/R = 0$) approximation, inherently implying that its applicability for computing the diffraction field patterns is limited to the paraxial far-field region.

III. NUMERICAL EXPERIMENTS ON ILLUSTRATIVE EXAMPLES

Firstly, the illustrative metasurfaces are synthesized and assembled by geometrically different CAAs shown in Fig. 1. The specific process is as follows. For the monofocal and multifocal metasurfaces, under normal illumination of a Gaussian plane-wave, their phase distributions on the metasurfaces can be obtained from the superimposed propagating fields originating from the in-phase point sources supposed at the preset focal points. To approximate the desired phase distributions, the CAAs with high transmission and appropriate phase are picked out and then arranged at the corresponding spatial locations for synthetization of the desired metasurfaces. It is noted that the CAAs (as shown in Fig. 1) show excellent EM properties, such as high transmission coefficients (more than 0.85), full 2π phase coverage, wide-angle stability (more than 30 degrees), and polarization-independence [7]. Then, field patterns of the synthesized metasurfaces are numerically analyzed by the FDTD full wave solver, the GRS, the GHF, and the HP. Here, it should be pointed out that the diffraction fields are calculated by the discrete summation formulas instead of the surface integral formulas in Section II, where $E(r')$ is the product of the complex field from the field source and the transmission coefficient of unit cell, i.e., CAAs at its center (x', y', z'), and the infinitesimal $ds = P^2$ is the area occupied by CAAs. In addition, for all the FDTD full wave simulations, the EM fields are obtained numerically by the high-performance three-dimensional (3D) EM analysis software, namely, CST Microwave Studio. In order to ensure the accuracy of the three-dimensional (3D) full wave simulations, the maximum

mesh cell size of $\lambda/15$ and the minimum one of $(\lambda/15)/20$ at 40GHz are set to capture the minimum relevant geometrical features in the model and strong field gradients within the whole computational domain. Perfectly matching layers (PMLs) as the boundary conditions are applied in all directions. When extracting the simulation results, to eliminate the potential influence of the probe array, the complex fields are directly extracted from 3D field monitors.

In order to investigate the applicability and accuracy of the GRS, a transmission-type focusing metasurface consisting of geometrically different CAAs with ultrahigh NA = 0.96 and subwavelength $fd = 0.58\lambda_0$ for the near-field PMMW-FPA imaging at 35 GHz is first considered. When normally and obliquely (30 degrees) illuminated by a linearly polarized Gaussian plane-wave (e.g., y-polarization), its paraxial and non-paraxial converging field patterns and their key parameters defining the focal beam quality are calculated by the GRS, and compared with those extracted by the FDTD full wave solver, the GHF, and the HP. In addition, two holographic metasurfaces, involving both paraxial/non-paraxial and near-/far-field multifocal patterned fields, are constructed. Similar computation and comparison are performed.

A. THE MONOFOCAL METASURFACE OF ULTRAHIGH NA = 0.96

Assume that the metasurface is located on the $z = 0$ plane. As shown in Fig. 2 (a) the axial 2D intensity patterns and (c) the radial ones calculated by the FDTD full wave solver, GRS, GHF, and HP from left to right for the normal incidence case, within the subwavelength near-field region the axial and radial paraxial focusing field profiles on the y = 0 plane and z = 6 mm plane computed by the GRS, keep perfect agreement with the FDTD simulation ones. Here, z = 6 mm plane is the focal plane calculated by the FDTD full wave solver. Besides, the one-dimensional (1D) on-axis field intensities and their differences versus the FDTD simulation ones as shown in blue curves of Fig. 2 (b) in the axial direction and (d) in the radial direction, also confirm this point. Furthermore, the key parameters, such as the focal position (*FP*), the axial depth of focus (*DOF*), radial full width at half maximum in the x-direction (*FWHMx*) and in the y-direction (*FWHMy*), maximum normalized intensity on the specified plane relative to the maximum within the whole region of interest (*MNI*), are marked in the Fig. 2 and listed in Table 1. It clearly indicates that the GRS enables superior accuracy to evaluate the focal beam quality. However, as seen in Fig. 2 (a)–(d) and Table 1 for the normal incidence case, remarkable differences exist in axial and radial 2D field patterns, 1D on-axis field intensities and their differences, and the key focusing parameters between the HP/GHF and the FDTD full wave solver, especially within the evanescent area. Similar phenomenon can be observed in Fig. 2 (e)–(h) the axial and radial 2D/1D intensity patterns and in Table 1 the key focusing parameters for the oblique incidence case, i.e., non-paraxial case. The visualized 2D off-axis focusing
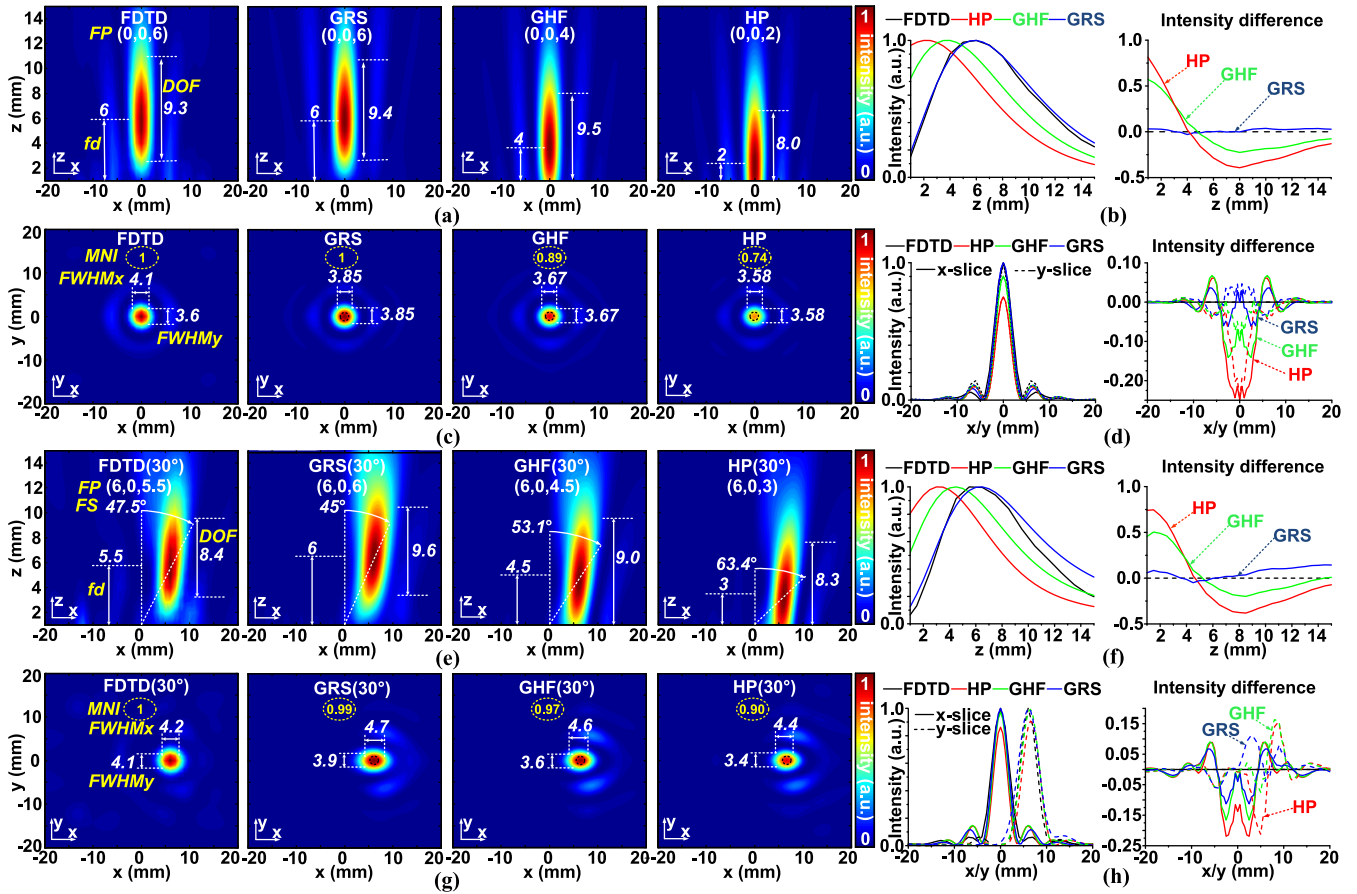
FIGURE 2. The simulated and numerical 2D/1D normalized intensities of the focusing metasurface with ultrahigh NA = 0.96 and *fd* = 6 mm illuminated by the y-polarization Gaussian plane-wave at incident angles of 0 and 30°. (a) and (e) The 2D axial intensity patterns, (b) and (f) the 1D axial intensities through the maximum points together with their differences versus the FDTD simulation ones on the y = 0 plane, (c) and (g) the 2D radial intensity patterns, and (d) and (h) the 1D radial intensities through the maximum points as well as their differences versus the FDTD simulation ones on the z = 6 mm and z = 5.5 mm plane, extracted by the FDTD full wave solver, GRS, GHF, and HP in the case of normal and oblique incidence, respectively. All white numbers inserted in Fig. 2 are in millimeters.

TABLE 1. The key focusing parameters characterizing the focal beam shape and quality (unit: mm).

Parameters	Normal incidence				Oblique incidence (30°)			
	FDTD solver	GRS	GHF	HP	FDTD solver	GRS	GHF	HP
FP	(0, 0, 6)	(0, 0, 6)	(0, 0, 4)	(0, 0, 2)	(6, 0, 5.5)	(6, 0, 6)	(6, 0, 4.5)	(6, 0, 3)
fd	6.0	6.0	4.0	2.0	5.5	6.0	4.5	3.0
FWHMx [a]	4.10	3.85	3.67	3.58	4.20	4.70	4.60	4.40
FWHMy [a]	3.60	3.85	3.67	3.58	4.10	3.90	3.60	3.40
DOF	9.3	9.4	9.5	8.0	8.4	9.6	9.0	8.3
MNI [a]	1	1	0.89	0.74	1	0.99	0.97	0.90
FS (°)	0	0	0	0	47.5	45.0	53.1	63.4

[a]*FWHMx, FWHMy, and MNI* indicate the focusing properties of the focal beam on the focal plane (z = 6 mm and z = 5.5 mm) determined by the FDTD full wave solver for the normal and oblique incidence case, respectively.

field patterns, 1D field intensities through the focuses and their differences versus the FDTD simulation ones, the radial focal shift (*FS*), and the key parameters further confirm that compared to the HP and the GHF, the GRS can more accurately map the non-paraxial near-field patterns to those

simulated by the FDTD full wave solver. Therefore, the above comparison results demonstrate that within the paraxial/non-paraxial subwavelength near-field region, the focusing metasurface of ultrahigh NA exemplifies that the GRS is capable of estimating the metasurface-modulating near-field patterns
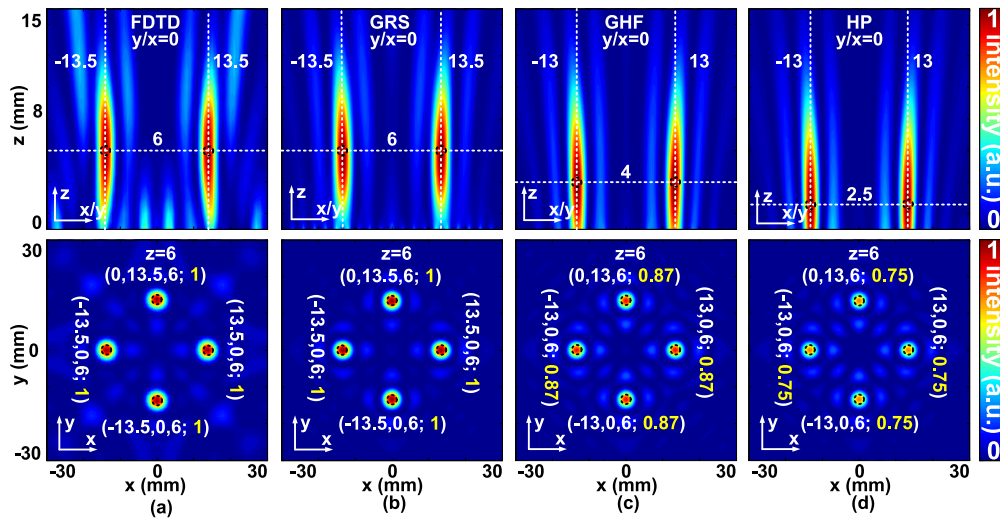
FIGURE 3. The axial and radial normalized intensity patterns on the y/x = 0 mm and z = 6 mm plane extracted by (a) the FDTD full wave solver, (b) the GRS, (c) the GHF, and (d) the HP for the coplanar multifocal holographic metasurface under normal illumination of a Gaussian plane-wave at 35 GHz. The yellow numbers inserted in Fig. 3 indicate the *MNI* at the denoted positions (the white numbers) on the z = 6 mm plane, respectively. All white numbers inserted in Fig. 3 are in millimeters.

TABLE 2. The key focusing parameters of the coplanar multifocal holographic metasurface (unit: mm).

Parameters	FDFD	GRS	GHF	HP
FP [a]	(0, ±13.5, 6)	(0, ±13.5, 6)	(0, ±13, 4)	(0, ±13, 2.5)
	(±13.5, 0, 6)	(±13.5, 0, 6)	(±13, 0, 4)	(±13, 0, 2.5)
fd	6	6	4	2.5
MNI [b]	1	1	0.87	0.75
	1	1	0.87	0.75

[a]*FP* indicates the focal positions of the four symmetrical focal spots in the y-direction and x-direction (up and down), respectively.
[b]*MNI* in the y-direction and x-direction (up and down) are calculated by the FDTD full wave solver, GRS, GHF, and HP on the z = 6 mm plane, i.e., the focal plane determined by the FDTD full wave solver.

with higher accuracy than the GHF and the HP, and provides excellent agreement with the full wave simulation results.

B. THE COPLANAR MULTIFOCAL HOLOGRAPHIC METASURFACE

Let us consider more complex multi-focus case to assess the capabilities of these methods. A holographic metasurface with its diameter of 54 mm covering four non-paraxial coplanar focal spots at (13 mm, 0 mm, 5 mm), (−13 mm, 0 mm, 5 mm), (0 mm, 13 mm, 5 mm), and (0 mm, −13 mm, 5 mm) within the evanescent region is assembled. Symmetrical multifocal field patterns in the axial and radial direction are calculated by the GRS and exhibited in the Fig. 3 (b), showing highly consistent with those from the FDTD full wave solver as shown in Fig. 3 (a). Especially in terms of the focal positions and relative intensities (the yellow numbers) on the z = 6 mm plane, the GRS provides better consistency with the full wave simulation ones than the GHF (Fig. 3 (c)) and the HP (Fig. 3 (d)), significant for holographic metasurface iterative inversion. To make it clearer, the above focusing

parameters, such as *FP*, *fd*, and *MNI* are extracted and listed in Table 2, also showing the superiority in precision of the GRS.

C. THE NON-COPLANAR MULTIFOCAL HOLOGRAPHIC METASURFACE

Finally, a non-coplanar multifocal holographic metasurface with its diameter of 54 mm and three focal spots at (0 mm, 0 mm, 5 mm), (12 mm, 0 mm, 8 mm), and (-20 mm, 0 mm, 20 mm), which covers both paraxial/non-paraxial and near-field/far-field scenarios, is adopted as a comprehensive example. The axial and radial intensity patterns are estimated by the above several methods and shown in Fig. 4. It is distinctly indicated that the diffraction intensity patterns on the y = 0 plane and on the cross sections of interest at z = 5 mm, z = 8 mm, and z = 20 mm estimated by the GRS are closer to the FDTD full wave simulation ones than the other two methods. Similarly, several local maximum points of the field intensity and their EM characteristics are marked in Fig. 4 and listed in Table 3. It is noted that in Table 3, *FP* and *MNI* of the
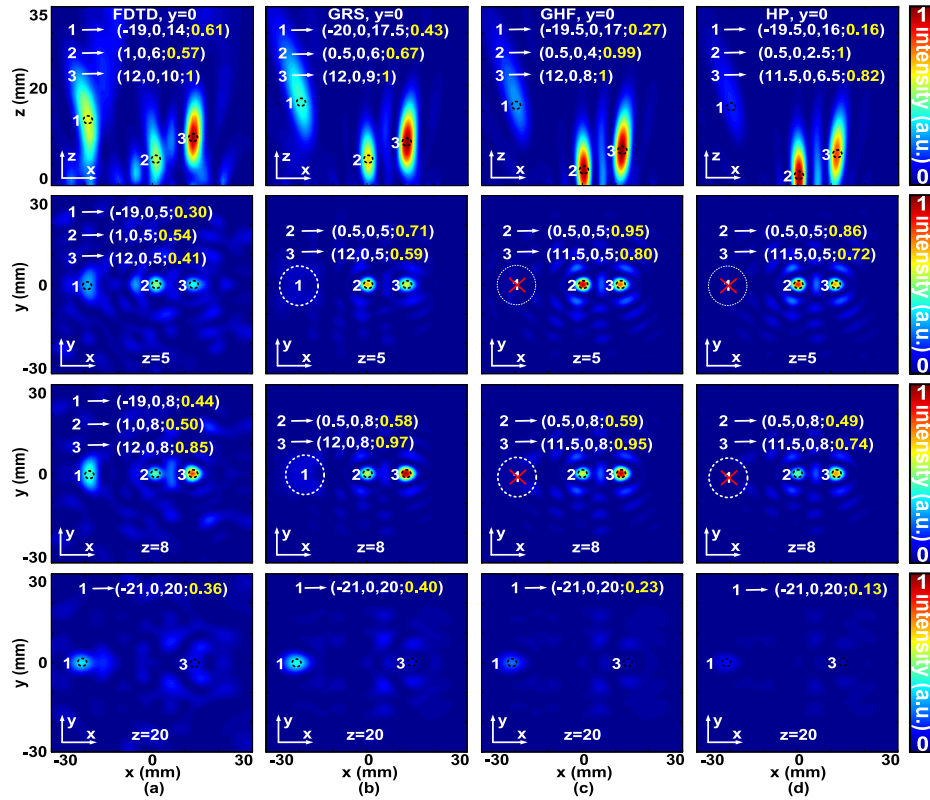
FIGURE 4. The axial and radial normalized intensity patterns on y = 0 plane and on the cross sections of interest at z = 5 mm, z = 8 mm, and z = 20 mm extracted by (a) the FDTD solver, (b) the GRS, (c) the GHF, and (d) the HP for the non-coplanar multifocal holographic metasurface under normal illumination of a Gaussian plane-wave at 35 GHz. The yellow numbers inserted in Fig. 4 indicate the *MNI* at the denoted positions (the white numbers) on the z = 5 mm, z = 8 mm, and z = 20 mm plane, respectively. All white numbers inserted in Fig. 4 are in millimeter.

TABLE 3. The positions of the local maximum points and their relative intensities (unit: mm).

Parameters	FDTD	GRS	GHF	HP
FP y = 0	(-19,0,14) (1,0,6) (12,0,10)	(-20,0,17.5) (0.5,0,6) (12,0,9)	(-19.5,0,17) (0.5,0,4) (12,0,8)	(-19.5,0,16) (0.5,0,2.5) (11.5,0,6.5)
MNI y = 0	0.61 0.57 1	0.43 0.67 1	0.27 0.99 1	0.16 1 0.82
FP z = 5 mm	(-19,0,5) (1,0,5) (12,0,5)	little (0.5,0,5) (12,0,5)	nothing (0.5,0,5) (11.5,0,5)	nothing (0.5,0,5) (11.5,0,5)
MNI z = 5 mm	0.30 0.54 0.41	little 0.71 0.59	nothing 0.95 0.80	nothing 0.86 0.72
FP z = 8 mm	(-19,0,8) (1,0,8) (12,0,8)	little (0.5,0,8) (12,0,8)	nothing (0.5,0,8) (11.5,0,8)	nothing (0.5,0,8) (11.5,0,8)
MNI z = 8 mm	0.44 0.50 0.85	little 0.58 0.97	nothing 0.59 0.95	nothing 0.49 0.74
FP z = 20 mm	(-21,0,20) nothing little	(-21,0,20) nothing little	(-21,0,20) nothing little	(-21,0,20) nothing little
MNI z = 20 mm	0.36 nothing little	0.40 nothing little	0.23 nothing little	0.13 nothing little

local maximum point 1, 2, and 3 on different planes are listed in each cell from top to bottom. And "nothing" and "little"

in Table 3 mean that there are nothing and greatly weak field at the denoted locations, respectively.

Furthermore, statistical data inserted in Fig. 4 and listed in Table 3, firmly confirm this point. Nevertheless, although the GRS shows fairly good agreement with the FDTD full wave solver, the differences between them in terms of the focus positions and their energy distribution ratios cannot be overlooked. It intuitively indicates that the amplitude and phase profiles modeled by the GRS are different from those presented by the metasurface in the FDTD full wave solver. This is mainly due to the fact that large gradient and irregular phase distributions required by the complex metasurface need to be implemented by the unit cells of increasing geometric differences, hence the mutational EM boundary among unit cells that are adjacent or close to each other on the metasurface finally results in uncertain phase jump and amplitude change. Unfortunately, it is not taken into account in the GRS like the full wave solver. Especially in this case, small aperture of 54 mm exactly aggravates these effects when generating three quite different non-coplanar focal spots. Therefore, it is demonstrated by the above examples that for a given metasurface as long as realistic EM response of each unit cell is exactly extracted, the GRS may provide accurate estimation of its diffraction fields either within the near-field region or within the far-field region.

In general, due to mutational boundary conditions among the geometrically different unit cells in the metasurface, unknown phase jump and amplitude change will reduce the accuracy of the proposed GRS. Nevertheless, the above cases show that the GRS can more accurately model the EM characteristics of the unit cells and trace the metasurface-modulating wavefront than the GHF and the HP, within the near-field region especially including the non-paraxial and evanescent area.

IV. CONCLUSION

In this paper, Huygens-Fresnel principle, Rayleigh-Sommerfeld diffraction theory, and Huygens' Principle for computing the metasurface-modulating field patterns are revisited and further reformulated. Then, we provide the generalized Rayleigh-Sommerfeld diffraction theory (GRS) by introducing a universal pattern-propagation Eigenfactor. Physical interpretation of GRS is supplemented. Typical and versatile numerical experiments are performed to demonstrate its capability to compute the metasurface-modulating non-paraxial near-fields accurately and efficiently. Compared to other advanced diffraction theory, GRS exhibits evident superiority in its wide applicability and greater accuracy of estimating the fields including evanescent and non-paraxial regions.

In general, the GRS improves the computational efficiency significantly and gives sufficiently accurate results compared to the time-consuming full wave analysis. It has potentially long-lasting impacts on the design and optimization of future metasurface-based devices, evolving towards multi-functionality and superior characteristics, including many important applications, e.g., subwavelength near-field imaging, holography, and single-photon detection, requiring accurate and efficient estimations of non-paraxial near-fields. Together with global optimization methods, the GRS may offer a universal design tool to fulfill this goal. Finally, it is emphasized that the GRS maintains its accuracy and efficiency across the entire spectrum from acoustics, microwave, terahertz, to optics.

REFERENCES

[1] H.-T. Chen, A. J. Taylor, and N. Yu, "A review of metasurfaces: Physics and applications," *Rep. Prog. Phys.*, vol. 79, no. 7, Jun. 2016, Art. no. 076401.

[2] F. Aieta, M. A. Kats, P. Genevet, and F. Capasso, "Multiwavelength achromatic metasurfaces by dispersive phase compensation," *Science*, vol. 347, no. 6228, pp. 1342–1345, May 2015.

[3] M. Khorasaninejad and F. Capasso, "Metalenses: Versatile multifunctional photonic components," *Science*, vol. 358, no. 6367, Dec. 2017, Art. no. eaam8100.

[4] F. Ding, A. Pors, and S. I. Bozhevolnyi, "Gradient metasurfaces: A review of fundamentals and applications," *Rep. Prog. Phys.*, vol. 81, no. 2, Aug. 2017, Art. no. 026401.

[5] T. Zvolensky, J. N. Gollub, D. L. Marks, and D. R. Smith, "Design and analysis of a W-band metasurface-based computational imaging system," *IEEE Access*, vol. 5, pp. 9911–9918, 2017.

[6] A. A. Fathnan and D. A. Powell, "Bandwidth and size limits of achromatic printed-circuit metasurfaces," *Opt. Express*, vol. 26, no. 22, pp. 29440–29450, Oct. 2018.

[7] H. Chu, J. Qi, S. Xiao, and J. Qiu, "A thin wideband high-spatial-resolution focusing metasurface for near-field passive millimeter-wave imaging," *Appl. Phys. Lett.*, vol. 112, no. 17, pp. 174101-1–174101-5, Apr. 2018.

[8] M. Juhl, C. Mendoza, J. P. B. Mueller, F. Capasso, and K. Leosson, "Performance characteristics of 4-port in-plane and out-of-plane in-line metasurface polarimeters," *Opt. Express*, vol. 25, no. 23, pp. 28697–28709, Nov. 2017.

[9] D. Lin, P. Fan, E. Hasman, and M. L. Brongersma, "Dielectric gradient metasurface optical elements," *Science*, vol. 345, no. 6194, pp. 298–302, Jul. 2014.

[10] D. Wen *et al.*, "Metasurface for characterization of the polarization state of light," *Opt. Express*, vol. 23, no. 8, pp. 10272–10281, Apr. 2015.

[11] Y. Chen, X. Yang, and J. Gao, "Spin-selective second-harmonic vortex beam generation with babinet-inverted plasmonic metasurfaces," *Adv. Opt. Mater.*, vol. 6, no. 19, pp. 1800646-1–1800646-8, Oct. 2018.

[12] X. Liu, I. V. Shadrivov, K. Fan, and W. J. Padilla, "Experimental realization of a terahertz all-dielectric metasurface absorber," *Opt. Express*, vol. 25, no. 1, pp. 191–201, Jan. 2017.

[13] J. Hao, J. Wang, X. Liu, W. J. Padilla, L. Zhou, and M. Qiu, "High performance optical absorber based on a plasmonic metamaterial," *Appl. Phys. Lett.*, vol. 96, no. 25, pp. 1104-1–1104-3, Jun. 2010.

[14] F. Cheng *et al.*, "Polarization-switchable holograms based on efficient, broadband multifunctional metasurfaces in the visible regime," *Opt. Express*, vol. 26, no. 23, pp. 30678–30688, Nov. 2018.

[15] Z.-L. Deng *et al.*, "Facile metagrating holograms with broadband and extreme angle tolerance," *Light, Sci. Appl.*, vol. 7, Oct. 2018, Art. no. 78.

[16] K. Achouri and C. Caloz, "Design, concepts, and applications of electromagnetic metasurfaces," *Nanophotonics*, vol. 7, no. 6, pp. 1095–1116, Jun. 2018.

[17] K. Wu, P. Coquet, Q. J. Wang, and P. Genevet, "Modelling of free-form conformal metasurfaces," *Nature Commun.*, vol. 9, no. 1, Aug. 2018, Art. no. 3494.

[18] C. L. Holloway and E. F. Kuester, "Generalized sheet transition conditions for a metascreen—A fishnet metasurface," *IEEE Trans. Antennas Propag.*, vol. 66, no. 5, pp. 2414–2427, May 2018.

[19] F. Elek, B. B. Tierney, and A. Grbic, "Synthesis of tensor impedance surfaces to control phase and power flow of guided waves," *IEEE Trans. Antennas Propag.*, vol. 63, no. 8, pp. 3956–3962, Sep. 2015.

[20] M. Chen, E. A.-Sánchez, A. Epstein, and G. V. Eleftheriades, "Theory, design, and experimental verification of a reflectionless bianisotropic Huygens' metasurface for wide-angle refraction," *Phys. Rev. B, Condens. Matter*, vol. 97, no. 12, pp. 125433-1–125433-14, Mar. 2018.

[21] J. Nagar, S. D. Campbell, and D. H. Werner, "Apochromatic singlets enabled by metasurface-augmented GRIN lenses," *Optica*, vol. 5, no. 2, pp. 99–102, Feb. 2018.

[22] Q.-W. Lin and H. Wong, "A low-profile and wideband lens antenna based on high-refractive-index metasurface," *IEEE Trans. Antennas Propag.* vol. 66, no. 11, pp. 5764–5772, Nov. 2018.

[23] Y. Zhou, X. Cao, J. Gao, H. Yang, and S. Li, "Reconfigurable metasurface for multiple functions: Magnitude, polarization and phase modulation," *Opt. Express*, vol. 26, no. 22, pp. 29451–29459, Oct. 2018.

[24] Q. He, S. Sun, S. Xiao, and L. Zhou, "High-efficiency metasurfaces: Principles, realizations, and applications," *Adv. Opt. Mater.*, vol. 6, no. 19, Oct. 2018, Art. no. 1800415.

[25] P. Ding, Y. Li, L. Shao, X. Tian, J. Wang, and C. Fan, "Graphene aperture-based metalens for dynamic focusing of terahertz waves," *Opt. Express*, vol. 26, no. 21, pp. 28038–28050, Oct. 2018.

[26] N. M. Estakhri, V. Neder, M. W. Knight, A. Polman, and A. Alu, "Visible light, wide-angle graded metasurface for back reflection," *ACS Photon.*, vol. 4, no. 2, pp. 228–235, Feb. 2017.

[27] S. A. Degtyarev, S. G. Volotovsky, and S. N. Khonina, "Sublinearly chirped metalenses for forming abruptly autofocusing cylindrically polarized beams," *J. Opt. Soc. Amer. B, Opt. Phys.*, vol. 35, no. 8, pp. 1963–1969, Aug. 2018.

[28] J. Zhao, H. Ye, K. Huang, Z. N. Chen, B. Li, and C.-W. Qiu, "Manipulation of acoustic focusing with an active and configurable planar metasurface transducer," *Sci. Rep.*, vol. 4, Sep. 2014, Art. no. 6257.

[29] M. Amin, O. Siddiqui, M. Farhat, and A. Khelif, "A perfect Fresnel acoustic reflector implemented by a Fano-resonant metascreen," *Appl. Phys. Lett.*, vol. 123, no. 14, pp. 144502-1–144502-9, Apr. 2018.

[30] A.-O. Diallo, R. Czarny, B. Loiseaux, and S. Holé, "Use of modified huygens-fresnel model to compute sub-wavelength dielectric antennas," in *IEEE MTT-S Int. Microw. Symp. Dig.*, May 2017, pp. 125–127.

[31] B. Orazbayev, V. Pacheco-Peña, M. Beruete, and M. Navarro-Cía, "Exploiting the dispersion of the double-negative-index fishnet metamaterial to create a broadband low-profile metallic lens," *Opt. Express*, vol. 23, no. 7, pp. 8555–8564, Apr. 2015.

[32] T. Hakkarainen, T. Setälä, and A. T. Friberg, "Subwavelength electromagnetic near-field imaging of point dipole with metamaterial nanoslab," *J. Opt. Soc. Amer. A, Opt. Image Sci.*, vol. 26, no. 10, pp. 2226–2234, Oct. 2009.

[33] N. W. Caira and D. R. Smith, "Multispectral metasurface hologram at millimeter wavelengths," *Appl. Opt.*, vol. 57, no. 1, pp. A19–A25, Jan. 2018.

[34] Z. Wang *et al.*, "Huygens metasurface holograms with the modulation of focal energy distribution," *Adv. Opt. Mater.*, vol. 6, no. 12, Jan. 2018, Art. no. 1800121.

[35] A. O. C. Davis, V. Thiel, M. Karpiński, and B. J. Smith, "Measuring the single-photon temporal-spectral wave function," *Phys. Rev. Lett.*, vol. 121, no. 8, Aug. 2018, Art. no. 083602.

[36] T. M. Bloomstein, M. F. Marchant, S. Deneault, D. E. Hardy, and M. Rothschild, "22-nm immersion interference lithography," *Opt. Express*, vol. 14, no. 14, pp. 6434–6443, Jul. 2006.

[37] P. Mehrotra, C. A. Mack, and R. J. Blaikie, "A solid immersion interference lithography system for imaging ultra-high numerical apertures with high-aspect ratios in photoresist using resonant enhancement from effective gain media," *Proc. SPIE*, vol. 8326, pp. 83260Z-1–83260Z-15, Mar. 2012.

[38] A. Pan, M. Zhou, Y. Zhang, J. Min, M. Lei, and B. Yao, "Adaptive-window angular spectrum algorithm for near-field ptychography," *Opt. Commun.*, vol. 430, pp. 73–82, Jan. 2019.

[39] M. Born and E. Wolf, "Elements of the theory of diffraction," in *Principles of Optics: Electromagnetic Theory of Propagation, Interference and Diffraction of Light*, vol. 4, 7th ed. Cambridge, U.K.: Cambridge Univ. Press, 1999, ch. 8, sec. 8.1-8, pp. 370–391.

[40] Y. Z. Umul, "Modified diffraction theory of kirchhoff," *J. Opt. Soc. Amer. A, Opt. Image Sci.*, vol. 25, no. 8, pp. 1850–1860, Aug. 2008.

[41] C. M. Roberts and V. A. Podolskiy, "Rigorous diffraction interface theory," *Appl. Phys. Lett.*, vol. 110, no. 17, pp. 171108-1–171108-5, Apr. 2017.

[42] H. H. Arsenault and P. García-Martínez, "Modern scalar diffraction theory," *Proc. SPIE*, vol. 8122, Aug. 2011, Art. no. 81220C.

HONGJUN CHU was born in Henan, China, in 1987. He received the B.S. degree in electronics and information engineering from Harbin Engineering University in 2010, and the M.S. degree in electromagnetic field and microwave technology from the Harbin Institute of Technology, Harbin, China, in 2015, where he is currently pursuing the Ph.D. degree in information and communication engineering. His research interests include metamaterials, passive millimeter-wave imaging technology, and millimeter-wave radar.
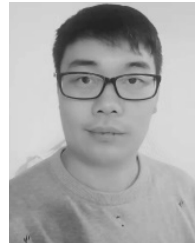
JIARAN QI received the Ph.D. degree in electromagnetics from Aalto University Finland, in 2011. From 2011 to 2012, he was a Postdoctoral Researcher with the Department of Radio Science and Engineering, Aalto University, Finland. He is currently an Associate Professor and the Vice Director with the Department of Microwave Engineering, School of Electronics and Information Engineering, Harbin Institute of Technology, Harbin, China.

He main research interests include metasurface-based mmW and THz imaging and detection, 5G massive MIMO, electromagnetic biological effect, and antenna technology.

RUI WANG was born in Inner Mongolia, China, in 1980. She received the B.S. degree in communication engineering from Jilin University, in 2003, and the M.S. degree in electromagnetic field and microwave technology from the Harbin Institute of Technology, in 2006.

From 2006 to 2013, she was an Engineer with the China Research Institute of Radio Wave Propagation. Since 2013, she has been a Senior Engineer. She has authored over 10 articles, and over 10 inventions. Her research interests include antenna theory and technology, the electromagnetic environment effect, and spectrum management.

JINGHUI QIU was born in Heilongjiang, China, in 1960. He received the B.S. degree in radio engineering, the M.S. degree in communication and information systems, and the Ph.D. degree in communication and information systems from the Harbin Institute of Technology in 1982, 1987, and 2008, respectively. From 1982 to 1987, he was a Teaching Assistant with the Harbin Institute of Technology. From 1987 to 1992, he promoted as a Lecturer, and then as an Associate Professor. He was promoted as a Professor, in 2002. He has authored and coauthored over 100 publications (book chapters, journal papers, and conference articles). His research interests include electromagnetic theory, microwave devices, antennas, and millimeter-wave imaging.

• • •